Journal of Chemical Health Risks
www.jchr.org
JCHR (2024) 14(5), 434-441 | ISSN:2251-6727

Bismuth Molybdate Supported on Graphitic Carbon Nitride Nanocomposite for Solar Driven Photodegradation with Enhancing Antibacterial and Antifungal Applications

Jayakumar Princy[1], Kuppusamy Krishnasamy[1]*
[1]Department of Chemistry, Annamalai University, Annamalai Nagar, Chidambaram - 608002, Tamil Nadu, India

(**Received**: 14 June 2024 **Revised**: 01 July 2024 **Accepted**: 18 August 2024)

Keywords:
$gC_3N_4/Bi_2(MoO_4)_3$; Hydrothermal method; Photocatalytic degradation; Antibacterial and antifungal.

ABSTRACT:
In this investigation, Graphitic carbon nitride wrapped bismuth molybdate nanocomposite has been synthesized efficiently to degrade the organic pollutants in water through the photodegradation process and to study their antibacterial and antifungal activities. Nanomaterials have been synthesized via hydrothermal method and antibacterial and antifungal properties are predicted using the disc diffusion method. The characterization of the synthesized materials viz., Bismuth molybdate and Graphitic carbon nitride loaded Bismuth molybdate nanomaterials were carried out using various techniques like X-ray diffraction, Field-emission Scanning electron microscopy and Energy dispersive X-ray, Transmission microscopy, X-ray photoelectron spectroscopy and ultraviolet spectroscopy. The photocatalytic performance of the samples under visible light was evaluated by observing the photodegradation of dye molecules. When compared to pure bismuth molybdate the loaded nanocomposite showed improved photocatalytic efficiency. Particularly, nanocomposite containing graphitic carbon nitride displayed the highest photocatalytic activity. Incorporating carbon nitride results in improved absorption of visible light and reduced recombination rates of photo-generated charge carriers. Furthermore, the prepared g-$C_3N_4/Bi_2(MoO_4)_3$ exhibited significant antibacterial and antifungal activities against four bacterial and two fungal strains. The developed method for preparing g-C_3N_4-based photocatalyst offers an encouraging approach to environmental remediation due to its convenience and cost-effectiveness. Moreover, the current research offers a novel nano-drug alternative.

1. INTRODUCTION

The fundamental cause of water pollution, which is still a serious and challenging crises globally, is human activity and the pollutants it produces which are essential to human survival. High quantities of insecticides, hydrocarbons, heavy metals, chemical waste, and persistent organic pollutants are among the contaminants that these sources release into water bodies. These pollutants pose serious environmental risks [1]. Industrial dyes are typically non-biodegradable or disintegrate slowly, necessitating treatment for contaminated water sources. They are difficult to remove because they are highly soluble and stable in water. The use of physicochemical processes is foundational to conventional wastewater treatment technology. Using semiconductors for photocatalysis, which breaks down contaminants using sunlight. This is an encouraging energetical strategy [2].

A promising green chemical process known as semiconductor-based photocatalysis uses sunlight as an energy source to break down contaminants and create hydrogen through water splitting [3]. Several studies used nano photocatalysts to treat dye-contaminated wastewater to remove colors from industrial wastewater. A wide range of nanomaterials, including titanium oxide, iron oxide, graphene nanocomposite, and metal sulfides, were extensively explored. Recent studies have demonstrated that ternary bismuth molybdate has an outwardly attractive visible light response, suitable band gaps, different ion conductivity, and photocatalytic characteristics [4]. Because of their unique properties, compounds containing bismuth have lately been explored as potential alternatives for commercial photocatalysts [5].

Journal of Chemical Health Risks
www.jchr.org
JCHR (2024) 14(5), 434-441 | ISSN:2251-6727

Bismuth oxides are commonly used to demonstrate effective, narrow-band-gap photo-catalytic materials [6]. In addition to its dielectric and gas sensor properties, it has lately demonstrated significant potential as a visible light-activated photocatalyst. [7].The graphitic carbon nitride (g-C_3N_4) has high thermal conductivity (600 °C), a small bandgap (2.7 eV) and excellent polymeric flexibility. Furthermore, g-C_3N_4 has been proposed as a significant metal free polymer material in a variety of photocatalytic applications due to its widespread availability via a thermal condensation process involving earth-abundant carbon/nitrogen-containing precursors namely melamine, urea, cyanamide, and thiourea [8].On the other hand, g-C_3N_4 has a relatively high conduction band position, resulting in a large reduction capability for its electron. This advantage stimulates the generation of superoxide radicals, hence enhancing the degradation efficiency. The selection of g-C_3N_4 as a modifier for $Bi_2(MoO_4)_3$ was based on its extensive surface area and short distance for carrier transfer [9]. $Bi_2(MoO_4)_3$, a heterostructured photocatalyst was synthesized and comprehensively detailed in this paper [10]. Under sunlight irradiation, the g-C_3N_4/$Bi_2(MoO_4)_3$ photocatalyst showed good photocatalytic efficiency in the breakdown of macromolecules as well as the highest zone of inhibition in biological activities. The chemical composition, morphological, optical quality, photocatalytic, antibacterial and antifungal activity were fully evaluated [11]. This research has been concentrated on the photodegradation of methylene blue by g-C_3N_4/$Bi_2(MoO_4)_3$ and pure $Bi_2(MoO_4)_3$, as well as their antibacterial and antifungal characteristics.

2. METHODOLOGY

2.1. *Chemicals*

Ammonium heptamolybdate $(NH_4)_6Mo_7O_{24}$, bismuth nitrate pentahydrate $Bi(NO_3)_3{\cdot}5H_2O$ and oxalic acid were purchased from Sigma Aldrich. All chemicals were used without undergoing further purification.

2.2. *Antibacterial and antifungal activity assay*

Disc diffusion method was used to assess the antibacterial and antifungal activities of Bismuth molybdate and Graphitic carbon nitride loaded Bismuth molybdate nanomaterials against a variety of bacteria and fungi, including two Gram-positive bacteria (*Staphylococcus aureus* and *Bacillus cereus*), two Gram-negative bacteria (*Escherichia coli* and *Salmonella typhii*) and two fungi (*Aspergillus* niger and *Candida albicans.*) pathogens.

2.3. *Preparation of g-C_3N_4*

The g-C_3N_4 was prepared by the thermal pyrolysis method. The melamine precursor is finally transformed to g-C_3N_4 at a calcination temperature of 550 °C for 3 hrs [12].

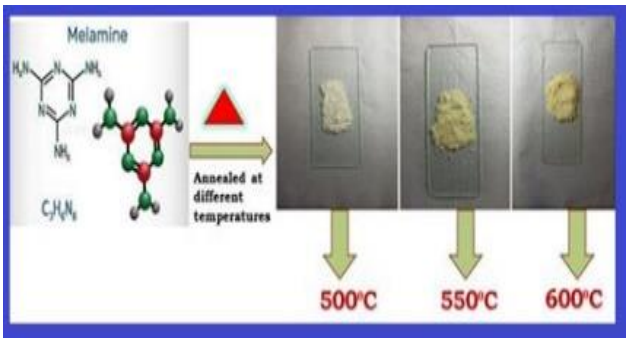

Figure 1. Preparation of graphitic carbon nitride

2.4. *Preparation of Bismuth Molybdate*

In a typical synthesis of bismuth molybdate, initially,1.7 g of ammonium heptamolybdate was dissolved in DI water and oxalic acid was added to above solution. After 10 minutes of stirring 0.8 g of bismuth nitrate pentahydrate was dissolved in double distilled water. After 30 minutes for the mixture to aerate, the solution was added drop wise to the Overnight, the solution was subjected to hydrothermal treatment at 120°C in a 100 ml autoclave walled with Teflon. The obtained precipitates were extensively rinsed with a mixture of ethanol and water. We calcined the leftovers at 550°C for 2 hours after drying them in an oven set at 80°C to generate the necessary $Bi_2(MoO_4)_3$ irregular nanospheres [13].

2.5. *Preparation of g-C_3N_4/Bismuth Molybdate*

The synthesis of g-C_3N_4/$Bi_2(MoO_4)_3$ began with 1.7g of ammonium heptamolybdate dissolved in double distilled water. Oxalic acid was added to the solution above. After ten minutes of rousing, 0.8 g of bismuth nitrate pentahydrate was added and 0.3 g of g-C_3N_4 was dissolved in double distilled water to the aforementioned solution and sonicated. Subsequently, the solution was added to the prior solution gradually while stirring continuously for thirty minutes. The resulting solution was subjected to hydrothermal treatment at 120°C in a 100 ml autoclave. The precipitates were extensively rinsed with a mixture of

Journal of Chemical Health Risks
www.jchr.org
JCHR (2024) 14(5), 434-441 | ISSN:2251-6727

ethanol and water. Precipitates were dried in an oven at 90℃ and calcined at 550℃ for 2 hours to get the required g-C_3N_4/$Bi_2(MoO_4)_3$ nanopetals[14].

3. RESULTS AND DISCUSSION

3.1. *XRD Analysis*

In Figure 2a, the XRD patterns of the prepared graphitic carbon nitride (g-C_3N_4) at different annealing temperatures displayed two inherent peaks at 13.2° and 27.6° corresponding to the (100) and (002) planes, which is well matched with the g-C_3N_4 Card no 87-1526. Figure 2b shows the XRD diffraction of the resulting bismuth molybdate. All of the observed peaks corresponding to $Bi_2(MoO_4)_3$ and MoO_3

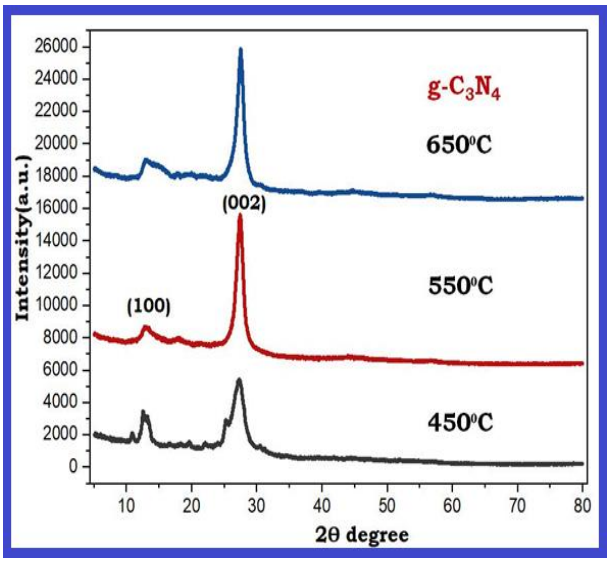

Figure 2 a. XRD pattern of g-C_3N_4 at different annealed temperatures

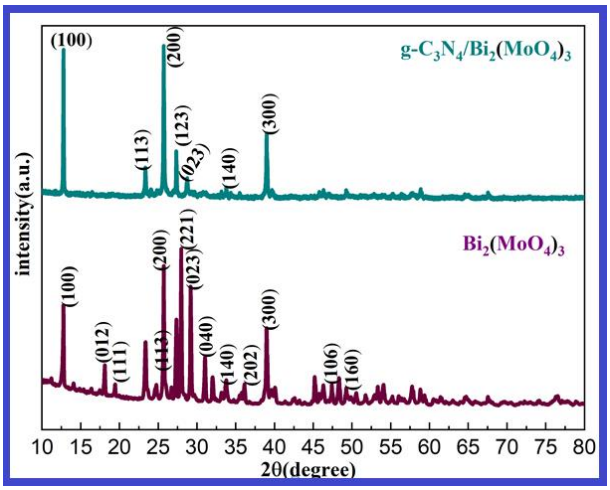

Figure 2 b. XRD Patterns of g-C_3N_4, $Bi_2(MoO_4)_3$ and g-C_3N_4/ $Bi_2(MoO_4)_3$

are well matched with JCPDS files 70-1396 and 76-1003, respectively. The absence of peaks attributable to Bi_2O_3 and other phases of Bi and Mo oxides implies that $Bi_2(MoO_4)_3$ has completely formed and coexists with excess MoO_3. Distinctive diffraction peaks observed for $Bi_2(MoO_4)_3$ at 12.82°, 18.11°, 19.43°, 24.71°, 25.65°, 27.65°, 28.10°, 29.24°, 31.12°,33.76 °,36.22°,39.83°, 48.29°, 49.23°, 52.63°,58.85°can corresponding to (100), (012) (111), (102), (200), (123) (221), (023), (040), (202), (300),(106),(160),(400),(116) crystal planes and well matched with JCPDS card no. 70-1396 and no attribute peaks of other contaminants can be detected in g-C_3N_4/$Bi_2(MoO_4)_3$. The crystalline size was calculated using the Scherrer equation [15].

$$D = 0.9n\lambda/\beta\cos\theta \quad (1)$$

The crystalline size of g-C_3N_4 was measured by applying the Debye Scherrer equation at 450,550 and 650° C and found to be 11.6, 4.3, and 5.8 nm respectively. The crystalline size of bismuth molybdate and graphitic carbon nitride anchored bismuth molybdate were calculated and found to be 23 and 22 nm respectively. No other peaks were presented in the synthesized materials which confirms the purity of the material.

3.2. *Morphological analysis*

Field emission scanning electron microscopy was used to characterize g-C_3N_4, bismuth molybdates, and g-C_3N_4/bismuth molybdates (Figure 3a, b, and c). Figure 3a reveals that pure g-C_3N_4 particles were irregular and had an exfoliated nanolayer structure. The as-prepared $Bi_2(MoO_4)_3$ is an agglomeration of irregular spherical-shaped material. Figure 3c shows the morphology of the g-C_3N_4/Bismuth molybdates composite, which resembles heterostructured nano petals with a length of 1μm. Moreover, the EDX spectrum exhibited the expected elements presented in the prepared nanocomposites. The elements C, and N only show in the g-C_3N_4 metal-free polymeric material. Bi, Mo,O and Bi, Mo,O,C,N elements exhibited the prepared bismuth molybdates and g-C_3N_4/bismuth molybdates respectively. This result indicates the purity of the prepared nanocomposites [16]. Transmission electron microscopy (TEM) spectra were employed to further investigate the composite's structure. Figure 4a shows the TEM images of pure g-C_3N_4 with a thin nanolayered structure. Figure 4(b) SAED pattern

Journal of Chemical Health Risks
www.jchr.org
JCHR (2024) 14(5), 434-441 | ISSN:2251-6727

exactly proved the amorphous nature of the material and the hkl (002) and (100) values well corroborate with the XRD pattern. The calculated interplanar d spacing values are 0.18nm and 0.2nm(Figure 4c). Furthermore, $Bi_2(MoO_4)_3$ nanoparticles are dispersed throughout the graphitic material nanolayered structure. The g-C_3N_4 nanolayer sheet is bonded to the area of $Bi_2(MoO_4)_3$, as shown in Figure 4(d), resulting in tight connections showing the distribution of g-C_3N_4 nanolayers on the surface of the bismuth molybdate sphere is demonstrated by TEM micrographs of the allocation of Bi, Mo, and O, which is consistent with the TEM analysis.

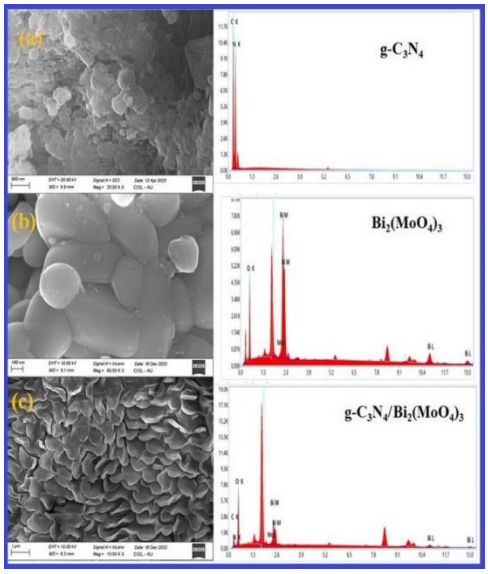

Figure 3a.FE-SEM micrograph and EDX spectrum of g-C_3N_4 ; **3b.**FE-SEM micrograph and EDX spectrum of $Bi_2(MoO_4)_3$ and **3c.**FE-SEM micrograph and EDX spectrum of g-C_3N_4/ $Bi_2(MoO_4)_3$

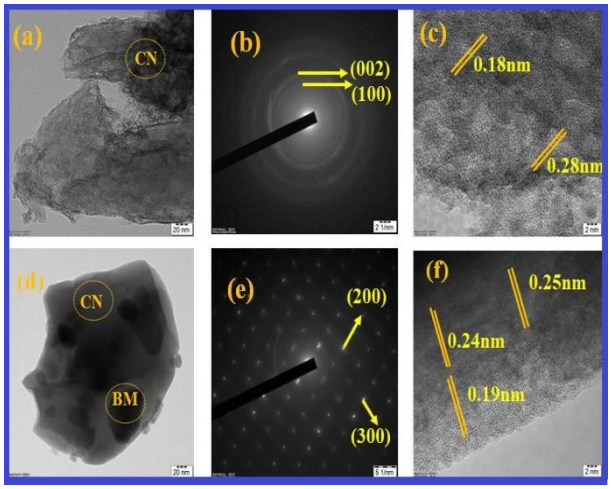

Figure 4a.TEM micrographs of g-C_3N_4,**Figure 4b.**SAED pattern of g-C_3N_4 and **Figure4c.**Lattice fringes of g-C_3N_4 ; **Figure 4d.**TEM micrographs of g-C_3N_4/$Bi_2(MoO_4)_3$ **,Figure 4e.**SAED pattern of g-C_3N_4/ $Bi_2(MoO_4)_3$ and **Figure4f.**Lattice fringes of g-C_3N_4/ $Bi_2(MoO_4)_3$.

Numerous irregularly shaped bismuth molybdate particles are dispensation on the surface of g-C_3N_4. Figure 4(e) SAED pattern of g-C_3N_4/bismuth molybdate spotted the bright spots exhibiting the polycrystalline nature of the material and the hkl(200) and (300) values well correlate with the XRD pattern. The calculated interplanar d spacing values of the prepared Nano petal g-C_3N_4/bismuth molybdate are 0.19nm,0.25nm, and 0.24nm respectively in lattice fringes (Figure 4f). This demonstrates that the g-C_3N_4/$Bi_2(MoO_4)_3$ composite was successfully synthesized [17].

3.3. *XPS Analysis*

X-ray photoelectron spectroscopy, the specific ionic states, and the elemental surface were verified. Figure 5 portrays the overall survey spectrum of as-prepared g-C_3N_4/Bismuth molybdates and reveals that no further elements can be found besides Bi, O, Mo, C, and N. The Bi $4f_{5/2}$ and Bi $4f_{7/2}$ spin orbitals binding energy peaks

Journal of Chemical Health Risks
www.jchr.org
JCHR (2024) 14(5), 434-441 | ISSN:2251-6727

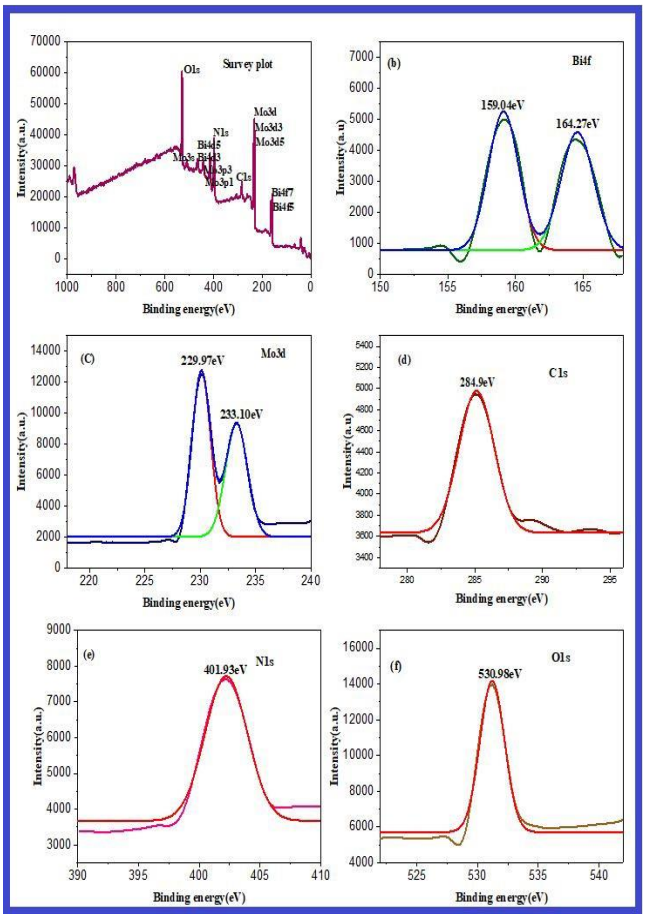

Figure 5. XPS spectra of g-C_3N_4/ $Bi_2(MoO_4)_3$

were observed at 159.04 eV and 164.27 eV, also the binding energy of Mo-3d illustrates peaks values of 229.97 eV and 233.10 eV in Figure 5, exhibited the high deconvoluted peak related to the $Mo3d_{5/2}$ and $Mo3d_{3/2}$, respectively. From the O 1s peak displayed the characteristic peak at the binding energy of 530.98 eV are related to the presence of lattice oxygen, and adsorbed oxygen molecules. The N 1s peak displayed at the binding energy of 401.93 eV is assigned to graphitic nitrogen and the C-1s peak appears at 284.9 eV due to carbon sp^2 C=C [18]. This result suggests the g-C_3N_4 was successfully combined with the bare material.

3.4. *Ultraviolet-visible diffuse reflectance spectroscopy*

In Figure 6a, we can observe the UV-Vis diffuse reflectance spectra of Graphitic carbon nitride, bismuth molybdate, and carbon nitride wrapped bismuth molybdate. The Kubelka-Munk plot is also used to measure their band gap (Eg) calculation. The hybrid samples demonstrate a little absorption redshift relative to pure $Bi_2(MoO_4)_3$, indicating that the sensitivity to visible light has been effectively enhanced through hybridization with g-C_3N_4. Consequently, the absorption of visible light is effectively caused by the g-C_3N_4/$Bi_2(MoO_4)_3$ band gap, which is 3.23 eV, The graphitic carbon nitride and bismuth molybdate energy gap values are 2.74 eV and 3.1 eV, respectively [19].

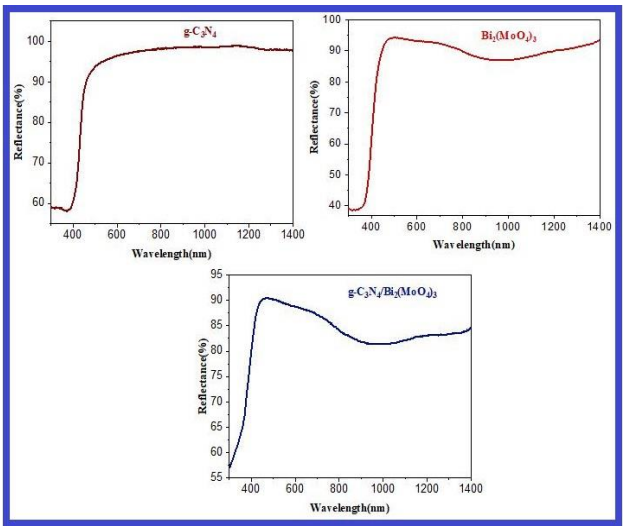

Figure 6a. UV-DRS spectra of prepared nanomaterials

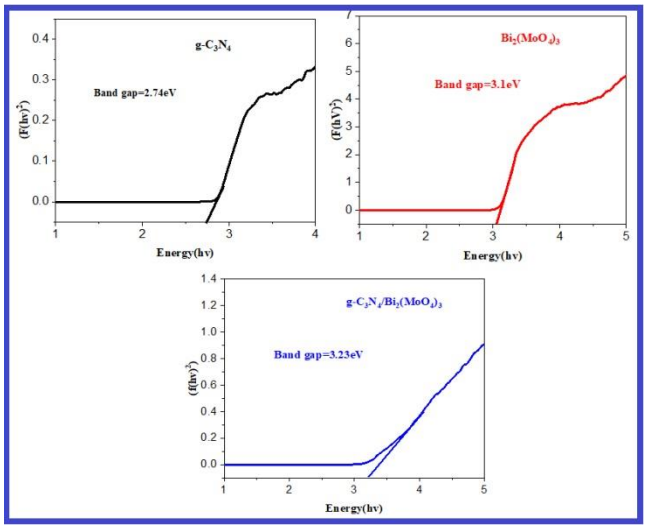

Figure 6b. Bandgap values of prepared nanomaterials

3.5. *Photocatalytic studies*

In photoactive synthesized catalysts assessed about MB dye degradation in an aqueous solution under solar light. There was no discernible deterioration, as the dark and photolysis (blank) reactions demonstrated. On the other hand, considerable deterioration was seen in the photocatalytic reaction employing artificial catalysts. The values of the rate constant were highest for the g-

Journal of Chemical Health Risks
www.jchr.org
JCHR (2024) 14(5), 434-441 | ISSN:2251-6727

$C_3N_4/Bi_2(MoO_4)_3$. Thus, enhancing photocatalytic activity involves forming a heterojunction with the appropriate semiconductors to lower the rate of recombination and charge transfer resistance. MB dye degradation is inured to gauge the produced nanoparticles degradation efficiency in the presence of sunshine. There are prominent absorption peaks in the MB at 600 and 700 nm(Figure 7). The degradation of the prepared nanomaterials with MB dye was monitored by observing changes in the dye's absorption maximum during the reaction, which are shown in Figures 7a and 7b. The catalyst was added to the MB dye solution, and the extent of degradation was tracked using changes in the absorption spectra at various time intervals. After a given irradiation time, ~5 mL aliquots of dye solutions were collected and examined at 600 to 700 nm in a Hewlett-Packard 8453 UV-vis spectrophotometer (USA). Among them, g-$C_3N_4/Bi_2(MoO_4)_3$ performed better in dye degradation ability (70%) than $Bi_2(MoO_4)_3$ [20]. According to the observation, the dyes break down into CO_2, H_2O, and non-absorbing substances like formates and acetates.The g-C_3N_4 supporting material plays an important role. One possible explanation is that g-C_3N_4 activates the active sites of bismuth molybdate, which in turn improves the efficiency of charge separation and inhibits the formation of (e^-) and (h^+) pairs. It was determined that the $gC_3N_4/Bi_2(MoO_4)_3$ catalyst significantly enhanced its photocatalytic activity.

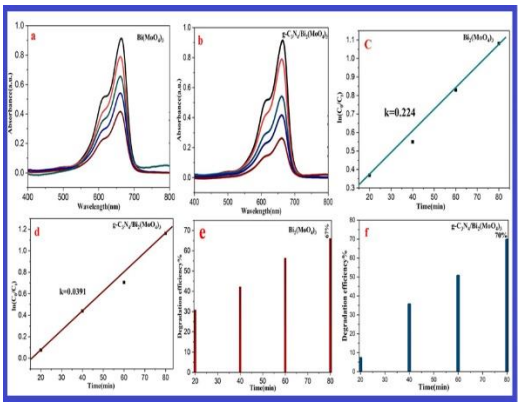

Figure 7. (a) and (b) Time-dependent UV-Vis absorption spectra of the photocatalytic degradation of MB dye ; (c) and (d) Plot of ($ln(C_0/C_t)$ versus time(min) ; (e) and (f) Degradation efficiency.

3.5.1. *Mechanism*

The experiment investigated the photocatalytic properties of g-$C_3N_4/Bi_2(MoO_4)_3$ under visible light exposure. According to the findings, potential photocatalytic pathways are outlined in Figure 8. When subjected to appropriate light, catalysts prompt agitation of electrons (e^-) from the valence band to the conduction band. Concurrently, an equal number of photogenerated holes (h^+) are generated in the valence band. When (e^-) and (h^+) are exchanged, reactions called photo-reduction and photo-oxidation are set in motion, which ultimately contribute to the breakdown of pollutants.

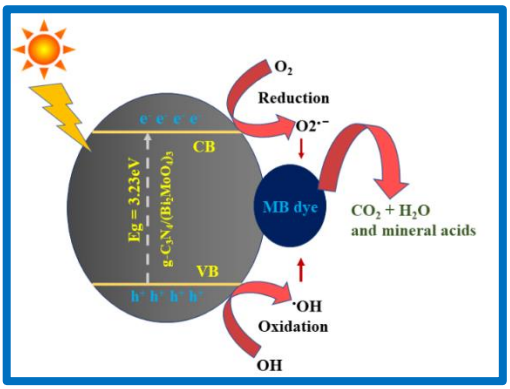

Figure 8. Pathway of dye degradation in the presence of photocatalyst.

3.6. *Antibacterial and Antifungal activity of prepared nanomaterials*

Antibacterial and antifungal effectiveness is determined using the disc diffusion method, and the results are discussed as follows. The test findings are displayed in Table S1. $Bi_2(MoO_4)_3$ demonstrated the most potent antibacterial activity against the four bacterial pathogens that were examined. The antibacterial efficacy against *Staphylococcus aureus* is 9 ±1.25mm compared to the standard which is 12 ±0.1mm. For *Escherichia coli*, the efficacy is 10 ±1.5mm compared to the standard drug which is 14± 0.03mm. *Bacillus cereus* shows an efficacy of 8 ±0.58mm compared to the normal medication which is 15 ±0.4mm. *Salmonella typhii* has an efficacy of 9± 3.45mm compared to the standard drug which is 13± 0.2mm. The $Bi_2(MoO_4)_3$ nanoparticles readily interact with microbes, effectively limiting their growth and so serving as potent antibacterial agents. $Bi_2(MoO_4)_3$ demonstrated superior antifungal effectiveness against *Aspergillus niger* (5±1.5mm) and Candida albicans (8±0.2mm) compared to conventional medications. The diameter of *Aspergillus niger* is 6±0.16 mm, while

the diameter of *Candida albicans* is 7±0.112 mm. The g-C_3N_4/ $Bi_2(MoO_4)_3$ compound exhibits significant

Journal of Chemical Health Risks
www.jchr.org
JCHR (2024) 14(5), 434-441 | ISSN:2251-6727

antibacterial activity against four different bacterial species: *Staphylococcus aureus* (10±0.1mm), *Escherichia coli* (9±0.5mm), *Bacillus cereus* (9±0.2mm), and *Salmonella typii* (10±1.3mm).

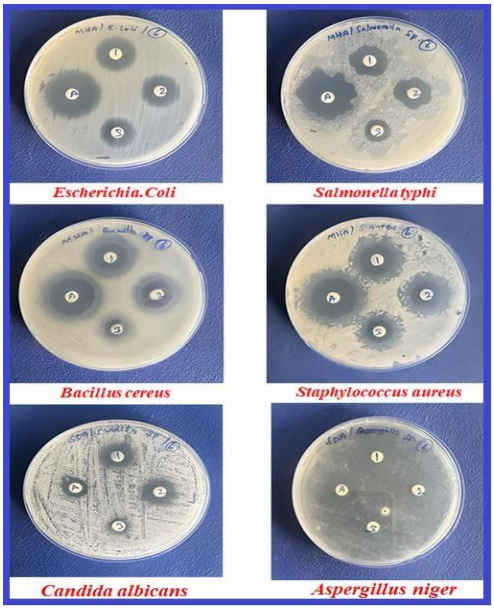

Figure 9. Antibacterial and Antifungal activity of $Bi_2(MoO_4)_3$

These values are compared to the standard drug, which has antibacterial activity of 12±0.2mm, 14±0.03mm, 15±0.4mm, and 13±0.2mm against the respective bacterial species.

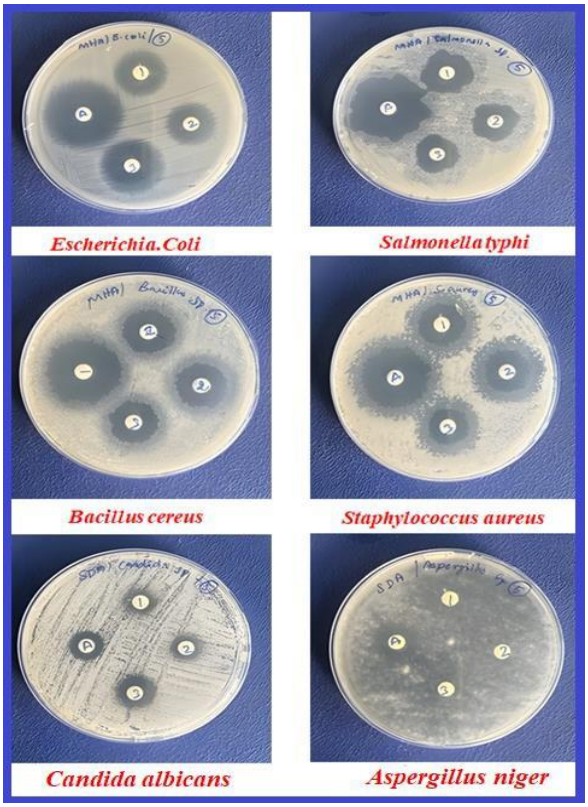

Figure 10. Antibacterial and Antifungal activity of g-$C_3N_4/Bi_2(MoO_4)_3$

Additionally, the compound shows antifungal activity against Aspergillus niger (4±0.18mm) and Candida albicans (7±0.112mm) (Figureure.9 and 10). The microbiological analysis revealed that both the prepared nanomaterials exhibit exceptional antibacterial activity against *Staphylococcus aureus* and antifungal activity against *Candida albicans* infections [21].

4. CONCLUSION

Hydrothermally synthesized heterojunction photocatalysts were extensively studied using XRD, UV-DRS, XPS, TEM, and SEM/EDS studies. The degradation effectiveness of the produced catalysts was examined by breaking down MB in the presence of solar light. Compared to pure material the synthesized material g-$C_3N_4/Bi_2(MoO_4)_3$ demonstrated exceptional degradation efficiency. The calculated rate constant values of g-$C_3N_4/Bi_2(MoO_4)_3$ are higher. The microbiological results showed that the synthesized nanomaterials have superior antibacterial activity against *Staphylococcus aureus* and antifungal activity against *Candida albicans* infections. The successful formation of heterostructured nanomaterials gives new insight into numerous

Journal of Chemical Health Risks
www.jchr.org
JCHR (2024) 14(5), 434-441 | ISSN:2251-6727

environmental remediation and its plays a vital role in potent drugs for antimicrobial and antifungal.

ACKNOWLEDGEMENT

The author thanks RUSA 2.0 for the financial support and The Department of Chemistry, Annamalai University for providing the necessary facilities to carry out this research.

REFERENCES

1. Li, N., Gao, H., Wang, X., Zhao, S., Lv, D., Yang, G.,Ge, L. 2020. Novel indirect Z-scheme g-C3N4/Bi2MoO6/Bi hollow microsphere heterojunctions with SPR-promoted visible absorption and highly enhanced photocatalytic performance. Chin J Catal. 41(3), 426-434.
2. Huo, T., Ba, G., Deng, Q., Yu, F., Wang, G., Li, H., & Hou, W. 2021. A dual strategy for synthesizing carbon/defect comodified polymeric carbon nitride porous nanotubes with boosted photocatalytic hydrogen evolution and synchronous contaminant degradation. Appl. Catal. B: Environ, 287, 119995.
3. Ajiboye, T. O., Oyewo, O. A., & Onwudiwe, D. C. 2021. Adsorption and photocatalytic removal of Rhodamine B from wastewater using carbon-based materials. FlatChem, 29, 100277.
4. Krishnapandi, A., Muthukutty, B., Chen, S. M., Arul, K. T., Shiuan, H. J., Selvaganapathy, M. 2021. Bismuth molybdate incorporated functionalized carbon nanofiber as an electrocatalytic tool for the pinpoint detection of organic pollutants in life samples. Ecotoxicol.Environ. Saf. 209, 111828.
5. Zargazi, M., & Entezari, M. H. 2020. Bi2MoO6 nanofilms on the stainless steel mesh by PS-PED method: Photocatalytic degradation of diclofenac sodium as a pharmaceutical pollutant. Ultrason. Sonochem. 62, 104867.
6. Cheng, L., Zhang, H., Li, X., Fan, J., & Xiang, Q. 2021. Carbon–graphitic carbon nitride hybrids for heterogeneous photocatalysis. Small, 17(1), 2005231.
7. Hussain, A., Lin, C., Cheruiyot, N. K., Huang, W. Y., Lin, K. S., & Hussain, A. 2022. Bismuth sulfide doped in graphitic carbon nitride degrades nitric oxide under solar irradiation. Nanomaterials, 12(19), 3482.
8. Chen, C., Wang, Y., Yi, Z., Wang, S., Ma, J., Gao, H., Yang, H. 2022. PH-induced structural evolution, photodegradation mechanism and application of bismuth molybdate photocatalyst. Adv. Powder Technol. 33(12), 103858.
9. Li, Y., Li, X., Zhang, H., Fan, J., & Xiang, Q. 2020. Design and application of active sites in g-C3N4-based photocatalysts. J. Mater. Sci. Technol. 56, 69-88.
10. Vasanthakumar, V., Alsawalha, M., Alomayri, T., Allehyani, S., Hu, Y. B., Fu, M. L., & Yuan, B. 2022. α-Bi2 (MoO4) 3 nanorods decorated with two-dimensional g-C3N4 nanosheets for efficient degradation of doxycycline under visible light illumination. Process Saf. Environ. Prot, 163, 1-13.
11. Jatav, S., Liu, J., Herber, M., & Hill, E. H. 2021. Facet engineering of bismuth molybdate via confined growth in a nanoscale template toward water remediation. ACS Appl. Mater Interfaces. 13(16), 18713-18723.
12. Rahman, A., Jennings, J. R., Tan, A. L., & Khan, M. M. 2022. Molybdenum disulfide-based nanomaterials for visible-light-induced photocatalysis. ACS omega, 7(26), 22089-22110.
13. Chen, Z., Zhang, S., Liu, Y., Alharbi, N. S., Rabah, S. O., Wang, S., & Wang, X. 2020. Synthesis and fabrication of g-C3N4-based materials and their application in elimination of pollutants. Sci. Total Environ. 731, 139054.
14. Phromma, S., Wutikhun, T., Kasamechonchung, P., Eksangsri, T., & Sapcharoenkun, C. 2020. Effect of calcination temperature on photocatalytic activity of synthesized TiO2 nanoparticles via wet ball milling sol-gel method. Appl. Sci. 10(3), 993.
15. Zhang, B., He, X., Ma, X., Chen, Q., Liu, G., Zhou, Y., Xin, Y. 2020. In situ synthesis of ultrafine TiO2 nanoparticles modified g-C3N4 heterojunction photocatalyst with enhanced photocatalytic activity. Sep. Purif Technol, 247, 116932.
16. Sathiyan, K., Bar-Ziv, R., Mendelson, O., & Zidki, T. 2020. Controllable synthesis of TiO2 nanoparticles and their photocatalytic activity in dye degradation. Mater. Res. Bull. 126, 110842.
17. Singh, J., Juneja, S., Soni, R. K., & Bhattacharya, J. 2021. Sunlight mediated enhanced photocatalytic activity of TiO2 nanoparticles functionalized CuO-Cu2O nanorods to remove methylene blue and oxytetracycline hydrochloride. J. Colloid Interface Sci. 590, 60-71.
18. Uribe-López, M. C., Hidalgo-López, M. C., López-González, R., Frías-Márquez, D. M., Núñez-Nogueira, G., Hernández-Castillo, D., & Alvarez-Lemus, M. A. 2021. Photocatalytic activity of ZnO nanoparticles and the role of the synthesis method on their physical and

chemical properties. J. Photochem.Photobiol. A: Chem. 404, 112866.

19. Okeke, I. S., Agwu, K. K., Ubachukwu, A. A., Madiba, I. G., Maaza, M., Whyte, G. M., & Ezema, F. I. 2021. Impact of particle size and surface defects on antibacterial and photocatalytic activities of undoped and Mg-doped ZnO nanoparticles, biosynthesized using one-step simple process. Vacuum, 187, 110110.

20. Pham, T. A. T., Tran, V. A., Le, V. D., Nguyen, M. V., Truong, D. D., Do, X. T., & Vu, A. T. 2020. Facile preparation of ZnO nanoparticles and Ag/ZnO nanocomposite and their photocatalytic activities under visible light. Int. J.Photoenergy, 2020, 1-14.

21. Deshmukh, S., Pawar, K., Koli, V., & Pachfule, P. 2023. Emerging graphitic carbon nitride-based nanobiomaterials for biological applications. ACS Appl. Bio Mater. 6(4), 1339-1367.